RSC Advances

PAPER

View Article Online
View Journal | View Issue

Cite this: *RSC Adv.*, 2025, **15**, 8244

Highly efficient oxidation of methane into methanol over Ni-promoted Cu/ZSM-5†

Zilong Shen,[a] Wenzhi Li, *[a] Jingting Jin,[a] Zhiheng Lu,[b] Liqun Wang,[a] Yihang Jiang[a] and Liang Yuan[b]

Received 15th February 2025
Accepted 10th March 2025

DOI: 10.1039/d5ra01115a

rsc.li/rsc-advances

Direct functionalization of methane in natural gas is of paramount importance but faces tremendous challenges. We reported a nickel-modified copper zeolite catalyst for the selective oxidation of methane into methanol. Using H_2O_2 as an oxidant in the liquid phase at 80 °C, $Cu_1Ni_{0.75}$/ZSM-5 catalyst presented a relatively high methanol yield of 82 162 μmol g_{cat}^{-1} h^{-1} (with a methanol selectivity of ~74%). Combining series of designed experiments and thorough characterization analysis, including electron microscopy, X-ray photoelectric spectroscopy, Fourier transform infrared reflection as well as *in situ* diffuse reflectance infrared Fourier transform spectroscopy, abundant Cu^{I} active sites were found on Ni-Promoted Cu/ZSM-5, differing from the dominating Cu^{II} active sites over Cu/ZSM-5. Cu^{I} active sites had an excellent ability to promote CH_4 adsorption, CH_4 activation and CH_3OH generation compared to Cu^{II} active sites. This work elucidates a constellation of insightful and potent perspectives for further improvement of metal-zeolite catalysts for the direct oxidation of methane to methanol.

1. Introduction

Methane is the major constituent of coalbed methane, natural gas, combustible ice, *etc.*, but has drawbacks of high storage cost and low calorific value as a fuel.[1,2] The highly efficient conversion of methane into commodity chemicals and liquid fuels,[3–5] especially its conversion into methanol (a clean liquid fuel suitable for transportation and storage),[6–8] has drawn extensive attention. The current industrial route is a two-step process, and depends on step-wise catalytic oxidation to synthesis gas, a mixture of H_2 and CO, which can react to form methanol ($CH_4 + H_2O \rightarrow CO + 3H_2$, $CO + 2H_2 \rightarrow CH_3OH$) under high temperature and pressure.[9,10] This process, however, is quite complicated and energy-intensive,[11] thus, the direct oxidation of methane to methanol under mild reaction conditions is urgently needed. Owing to the high carbon-hydrogen (C–H) bond energy (438.8 kJ mol^{-1}) in the non-polarized methane, direct oxidation of methane to methanol remains a major challenge.[12–14] A large number of noble metal catalysts (*e.g.*, AuPd@ZSM-5-C_{16},[15] AuPd nanocatalyst,[16] IrCuPd-ZSM-5,[17] GR-Rh/Ni (111) catalyst[18] and so on) have been proposed due to their excellent ability in methane activation. Moreover, a portion of researchers chose to design catalysts with unique active sites (*i.e.*, Cu/CN,[19] metal–organic framework (MOF),[20,21] Pd_xAu_y nanosheets[22]) to achieve efficient direct conversion of methane to methanol. Yet, these catalysts are either expensive to prepare or difficult to synthesize, which makes them unreliable for large-scale production.[23,24] Inspired by the biocatalytic enzyme systems in nature that can achieve direct methane to methanol conversion under mild conditions, metal-containing zeolites with the enzyme-like active Cu-oxo active sites have received great attention.[25–29]

In recent years, direct conversion of methane into methanol over the copper-exchanged zeolites such as Cu-MOR,[30] Cu-CHA,[11] Cu-ZSM-5,[31] using O_2,[11,30] N_2O[32] or H_2O_2 (ref. 31) as oxidant, has garnered significant interest. Sushkevich *et al.* achieved 97% methanol selectivity on Cu-MOR using water steam as the oxidant at 473–673 K.[30] Zhang *et al.* reported that Cu–OH single sites confined within the 6-membered ring (6 MR) voids of SSZ-13 zeolite exhibited high efficiency in continuous methane to methanol conversion using water as an oxidant at 400 °C. In addition, the bare Cu(II) single atom sites in 6 MR exhibited activity in methane C–H activation, while their stable four coordination structure hindered their reactivity at lower temperatures.[33] The direct conversion of methane in gas-phase systems mostly occurred under high-temperature conditions, which contradicts the intention to reduce energy consumption. Therefore, many researchers delved their interest into the low-temperature liquid-phase reaction systems, using H_2O_2 as an oxidant. Jin *et al.* used copper oxysalt as the precursor to prepare Cu/ZSM-5 by calcination method, on which the methanol yield exhibited a special M-shaped curve with the highest yield of 15 975.73 μmol g_{cat}^{-1} h^{-1}.[31] Nevertheless, single

[a]*Laboratory of Clean Low-Carbon Energy, Department of Thermal Science and Energy Engineering, University of Science and Technology of China, Hefei 230023, P. R. China. E-mail: liwenzhi@ustc.edu.cn*

[b]*National & Local Joint Engineering Research Center of Precision Coal Mining, Anhui University of Science and Technology, Huainan 232001, P. R. China*

† Electronic supplementary information (ESI) available. See DOI: https://doi.org/10.1039/d5ra01115a

metal catalysts may not be able to effectively distinguish methane from generated intermediates, resulting in increased side reactions and decreased methanol selectivity. In the process of methane conversion, it is necessary to construct more refined active sites to improve the overall efficiency.

It was found that bimetallic catalysts have superior ability to promote CH_4 activation and CH_3OH generation compared to monometallic catalysts. For example, Yu *et al.* reported a bimetallic catalyst (Cu–Fe(2/0.1)/ZSM-5), exhibiting a superior methanol yield of 431 mol_{MeOH} mol_{Fe}^{-1} h^{-1}, which is at least one order of magnitude greater than that of any catalysts previously reported.[34] Wang *et al.* elaborated that Pd and Cu synergistically disaggregated methane, which facilitated the formation of important intermediate (metal–CH_3) with a relatively higher CH_3OH yield of ~31 800 μmol g_{cat}^{-1} h^{-1}.[35] Yu *et al.* designed and constructed atomically dispersed Ag and Cu dual single atoms anchored on ZSM-5 through an improved co-adsorption strategy as an efficient catalyst to promote methane conversion. This work demonstrated that the synergistic effect between Ag and Cu single atoms anchored within the zeolite channels promoted the formation of highly active surface hydroxyl species to activate C–H bonds, and correspondingly enhanced the yield, selectivity, and stability.[36] Xu *et al.* found that regulating Au coverage on Pd_xAu_y nanosheets could control the energy barrier of the triggering step to obtain an excellent CH_3OH production rate of 147.8 mmol g_{Pd}^{-1} h^{-1}, with a CH_3OH selectivity of 98% at 70 °C.[22] However, the effect of bimetallic synergy on the direct conversion of methane into methanol is still a noteworthy issue. Moreover, most existing researches used noble metals to modify copper exchange zeolites, which were costly, thus, we plan to find a suitable non-noble metal modification pathway to promote Cu-zeolites' reactivity.

Herein, we noticed that the addition of Ni during the preparation process of Cu/ZSM-5 catalysts greatly increased the yield of methanol, while maintaining methanol selectivity, thus, we devised a series of Ni-Promoted Cu/ZSM-5 catalysts using ammonia evaporation method and were applied for direct oxidation of methane to methanol (DOMM) in the liquid phase using H_2O_2 as an oxidant at 80 °C. We found that Ni improved the CH_3OH yield of Cu/ZSM-5 catalysts. Therefore, a series of experiments and characterization methods (such as electron microscopy, spectroscopic techniques to *in situ* or *ex situ*, Electron Spin Resonance) were used to explain this phenomenon, from which we explained the reason why Ni promoted Cu/ZSM-5 catalysts: Ni promoted the conversion of Cu^{II} sites to Cu^{I} sites, while Cu^{I} sites had excellent ability to promote CH_4 adsorption, CH_4 activation and CH_3OH generation compared to Cu^{II} sites, and then discovered a possible free radicals pathway for the high-yield conversion of CH_4 to C1 products (CH_3OH and HCOOH).

2. Materials and methods

2.1. Catalyst preparation

The pretreatment of zeolite (HZSM-5):H-ZSM-5 was calcined at 500 °C with a heating ramp of 2 °C min^{-1} for 4 h in air.

Ammonia evaporation method: First, 1 mL of $NH_3 \cdot H_2O$ was added to 20 mL of deionized water dispersed with 1g of HZSM-5 support and stirred for 10 min. Once 5 mL of the required concentration of $Cu(NO_3)_2 \cdot 3H_2O$ and $Ni(NO_3)_2 \cdot 6H_2O$ solution was added, then sealed the suspension with Parafilm and stirred for 1 hour. Next, removed the Parafilm and evaporated the solvent at 90 °C for 1 hour. After obtaining the catalyst precursor through vacuum filtration, it was dried in an oven at 110 °C for 8 h. Finally, the sample was calcined at 500 °C with a heating ramp of 2 °C min^{-1} for 4 h in air. The obtained catalyst was denoted as Cu_xNi_y/ZSM-5 (x/y refers to the ratio of weight percentage of Cu/Ni). Cu_1/ZSM-5 refers to the sample with 1 wt% of Cu.

2.2. Catalyst testing

The methane oxidation was tested in a 100 mL stainless steel reactor. The vessel was loaded with an aqueous solution of H_2O_2 (40 mL, 0.5 M) and 10 mg of catalyst, purged three times with methane, and then charged with methane to 30 bar. The reaction mixture was heated to 80 °C while being stirred at a speed of 900 rpm and maintained under these conditions for a duration of 30 minutes. Upon completion of the reaction, the vessel was rapidly cooled using an ice-bath.

The gaseous phase products were further analyzed by a gas chromatograph (GC 5190) equipped with a thermal conductivity detector (TCD). The liquid products were quantified by ^{1}H-NMR on a 600 MHz JNM-ECZ600R/S1 Superconducting Fourier Nuclear Magnetic Resonance Spectrometer. Typically, 0.7 mL of the sample solution and 0.3 mL of D_2O were combined in an NMR tube. A solvent suppression program was employed to minimize the signal originating from the solvent. A representative example of ^{1}H NMR spectrum obtained from products of methane oxidation reaction is shown in Fig. S1.†

The CH_3OH yield, HCOOH yield, C1 yield and CH_3OH selectivity were calculated through the following equations:

$$\mathrm{CH_3OH\ yield}\left(\mu\mathrm{mol\ g_{cat}^{-1}\ h^{-1}}\right) = \frac{n[\mathrm{CH_3OH}]}{m[\mathrm{catalyst}]t[\mathrm{reaction\ time}]}$$

$$\mathrm{HCOOH\ yield}\left(\mu\mathrm{mol\ g_{cat}^{-1}\ h^{-1}}\right) = \frac{n[\mathrm{HCOOH}]}{m[\mathrm{catalyst}]t[\mathrm{reaction\ time}]}$$

$$\mathrm{C1\ yield}\left(\mu\mathrm{mol\ g_{cat}^{-1}\ h^{-1}}\right) = \frac{n[\mathrm{C1}]}{m[\mathrm{catalyst}]t[\mathrm{reaction\ time}]}$$

$$\mathrm{CH_3OH\ selectivity}(\%) = \frac{n[\mathrm{CH_3OH}]}{n[\mathrm{all\ products}]} \times 100\%$$

2.3. Catalyst characterization

The Transmission Electron Microscope (TEM) and High-Angle Annular Dark Field Scanning Transmission Electron Microscope (HAADF-STEM) mapping images were characterized by

two TEM instruments (JEM-2100F FETEM and FEI Talos F200S), which showed the morphology and surface crystal structure of the catalysts prepared in this article. The X-ray Diffraction (XRD) patterns were performed on a Rigaku SmartLab (9) Multifunctional Rotating-anode X-ray Diffractometer (Cu Kα) in the range of 5–60° with a step size of 0.02°, operated at 40 kV and 40 mA. The X-ray Photoelectron Spectroscopy (XPS) was performed using a Thermo Scientific ESCALAB 250Xi X-ray photoelectron spectrometer (Al Kα 150 W, $h\nu$ = 1486.6 eV). The binding energies were calibrated using C1s peak of contaminant carbon (BE = 284.8 eV) as an internal standard. The loading amounts of Cu and Ni were determined by the Inductively Coupled Plasma Optical Emission Spectrometer (ICP-OES) instrument. Before analysis, a proper amount of powder sample was treated with nitric acid to obtain a clear solution. The surface area and pore-size distribution of catalysts were tested through nitrogen adsorption and desorption method on a Micromeritics ASAP 2460 instrument using the BET equation and the BJH method, respectively. Additionally, adsorption/desorption isotherms for CH_4 in the catalysts were also measured. Fourier Transform Infrared Reflection (FT-IR) and *in situ* Diffuse Reflectance Infrared Fourier Transform Spectroscopy (DRIFTS) were analyzed on the NICOLET iS50 FT-IR spectrometer equipped with a MCT detector. High-performance Liquid Chromatography (HPLC) was used to test the yield of formic acid. 5,5-dimethyl-1-pyrroline N-oxide (DMPO) spin-trapping Electron Paramagnetic Resonance (EPR) experiments were conducted on a JES-FA 200 (JEOL) Electron Paramagnetic Resonance Spectrometer at room temperature. The samples (1 mL) after methane oxidation at 80 °C for 5 min were quickly collected and 1 mL DMPO solution (10 mg mL^{-1}) was added into the samples, and then filtered and frozen by liquid nitrogen. These samples were thawed subsequently for the EPR measurements.

3. Results and discussions

3.1. Catalytic performance

The CH_3OH yield, CH_3OH selectivity and CH_4 conversion rate over $Cu_1/ZSM\text{-}5$ and $Cu_1Ni_{0.75}/ZSM\text{-}5$ under different reaction conditions were tested. Methanol, formic acid, unreacted methane, hydrogen and oxygen produced by the decomposition of hydrogen peroxide could be detected through ^1H NMR and gas chromatograph equipped with a thermal conductivity detector.

The $Cu_xNi_y/ZSM\text{-}5$ catalysts which were prepared by ammonia evaporation method exhibited excellent catalytic performance for DOMM under the standard reaction conditions (x/y referred to the ratio of weight percentage of Cu/Ni and the actual loading amounts were shown in Table S1†). Only liquid phase products (CH_3OH and HCOOH) were detected after the DOMM reaction, and no gaseous phase products like CO and CO_2 were detected, indicating this catalyst have by-passed the unwanted over-oxidation (Fig. S2†). A volcano-like Ni loading-catalytic performance relationship was exhibited where the maximum catalytic activity appeared at $Cu_1Ni_{0.75}/ZSM\text{-}5$ with a CH_3OH yield of 82 162 μmol g_{cat}^{-1} h^{-1} and selectivity of 74% (Fig. 1A).

In the control experiment without methane or H_2O_2, there were no products. When no catalyst was added, there were still a trace amount of CH_3OH, which could resulted from the $^{\bullet}OH$ radicals generated by H_2O_2 spontaneous decomposition (Fig. S3†). For DOMM reaction over the pure HZSM-5 zeolite support, the CH_3OH yield was not significantly different from the situation without catalyst, which indicated that pure HZSM-5 zeolite support had merely catalytic effect on the DOMM reaction (Fig. S4†). For DOMM over $Cu_1/ZSM\text{-}5$ at 80 °C, the yield of CH_3OH was 73 050 μmol g_{cat}^{-1} h^{-1} (Fig. 1A), which was much higher than that of pure HZSM-5 zeolite support. Obviously, the load of Cu greatly promoted the DOMM reaction, which proved that Cu was the main active site of the reaction. However, when the Ni-Promoted Cu/ZSM-5 catalysts were used in the DOMM reaction, the yields of CH_3OH were further improved by 12.5% compared to the Cu/ZSM-5 catalysts, which showed that the addition of Ni improved the activity of Cu species over $Cu_1Ni_{0.75}/ZSM\text{-}5$ catalyst. Furthermore, in order to eliminate the possibility that the observed activity may only come from a combination of Ni and Cu active sites, and considering the quantities of Cu, Ni and ZSM-5 in both reaction systems should be equal, we used physically mixed $Cu_1/ZSM\text{-}5$ and $Ni_{0.75}/ZSM\text{-}5$ (10 mg each, reaction 6) and physically mixed $Cu_1Ni_{0.75}/ZSM\text{-}5$ and ZSM-5(10 mg each, reaction 7) as catalysts for the DOMM reaction to make a comparison (Table S2†). The yield of CH_3OH over the physically mixed $Cu_1Ni_{0.75}/ZSM\text{-}5$ and ZSM-5 (10 mg each) for DOMM was 857.22 μmol h^{-1}, which was 11.39% higher than that of the physically mixed $Cu_1/ZSM\text{-}5$ and $Ni_{0.75}/ZSM\text{-}5$. The above results distinctly suggested that there was a remarkable synergistic effect between Cu and Ni, which enhanced the catalytic activity.

To improve the reaction conditions for the catalytic conversion of methane using $Cu_1Ni_{0.75}/ZSM\text{-}5$ catalyst, a series of reaction conditions (such as CH_4 pressure, H_2O_2 concentration, and reaction temperature) were studied. The effect of the CH_4 pressure on the DOMM was firstly studied. With the increase of the CH_4 pressure, the yield of all products increased, specifically the CH_3OH selectivity also increased (Fig. 1B and Table S3†). Next, the H_2O_2 concentration was studied. Similar to CH_4 pressure, the H_2O_2 concentration was positively correlated with C1 yield. Even so, the CH_3OH selectivity possessed the opposite trend (Fig. 1C and Table S3†), evidencing that the $^{\bullet}OH$ radicals generated by H_2O_2 decomposition are crucial in the DOMM reaction as the increase in H_2O_2 will lead to excessive oxidation of CH_4 to HCOOH. Another important reaction condition is temperature, which would improve DOMM reaction (Fig. 1D).

In addition, the stability of catalysts was tested through cyclic experiments under the standard reaction condition (Fig. S5†). CH_4 was converted into CH_3OH at a rate ranging from 74 554 to 82 600 μmol g_{cat}^{-1} h^{-1} with a CH_3OH selectivity kept at 74–79%. Our best catalyst with Cu/Ni loadings at 1/0.75 wt% had a more excellent CH_3OH yield compared to other recently reported catalysts, which indicated that Ni-Promoted Cu/ZSM-5 catalyst showed promising application prospects in methane conversion under mild conditions (Fig. S6 and Table S4†). Above all, the $Cu_1Ni_{0.75}/ZSM\text{-}5$ catalyst could be considered as a stable and efficient catalyst for the DOMM reaction.

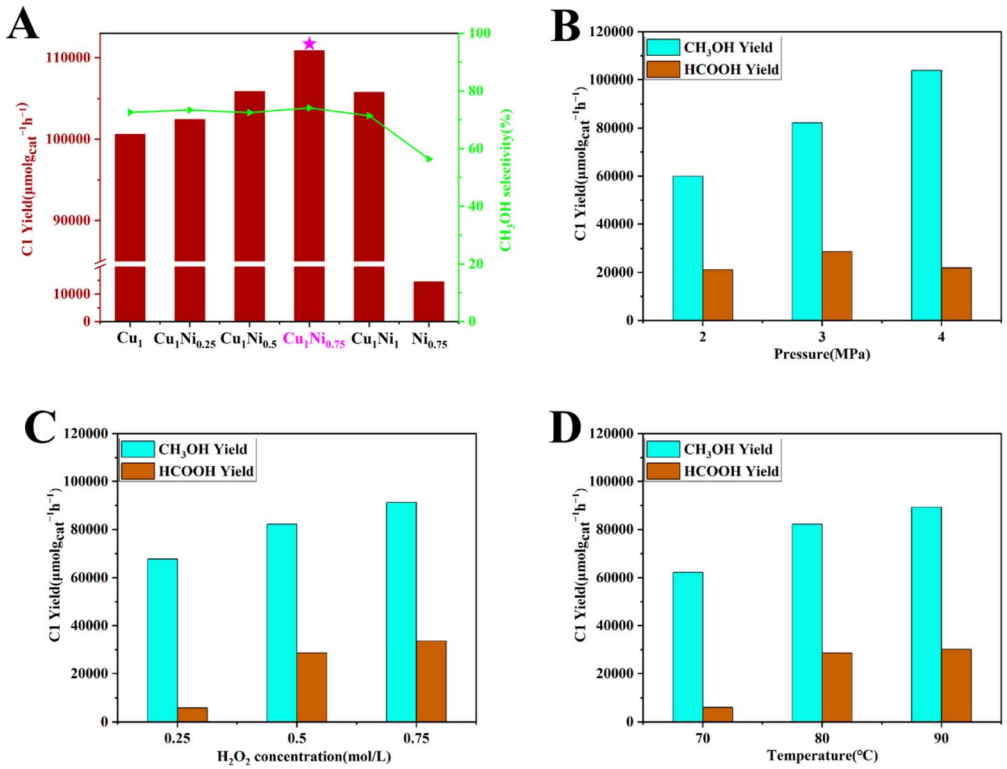

Fig. 1 Effect of (A) different Ni loading amounts on C1 yield and CH_3OH selectivity (Cu_xNi_y refer to Cu_xNi_y/ZSM-5 catalysts). Effect of (B) different CH_4 pressure, (C) H_2O_2 concentration, (D) reaction temperature on CH_3OH and HCOOH yield. Standard reaction conditions for this work unless otherwise stated were 38 mL H_2O, 2 mL 30% H_2O_2, feed CH_4 at 3.0 MPa, react at 80 °C for 30 min, and 10 mg Cu_xNi_y/ZSM-5 catalysts.

3.2. Structure characterization of catalysts

The activity of catalysts for methane conversion is closely related to their structure,[37] thus, a complete structure characterization of the Cu_xNi_y/ZSM-5 catalysts was in progress. First, XRD patterns of the different catalysts were shown (Fig. 2A). After the loading of metal (Cu and/or Ni), no metal peaks were detected (Cu_2O:JCPD Card 65-3288, CuO:JCPD Card 45–0937, Ni:JCPD Card 04-0850, NiO:JCPD Card 44-1159; the detailed comparison results were shown in the Fig. S7†).In addition, we could observe the uniform distribution of Cu and Ni elements

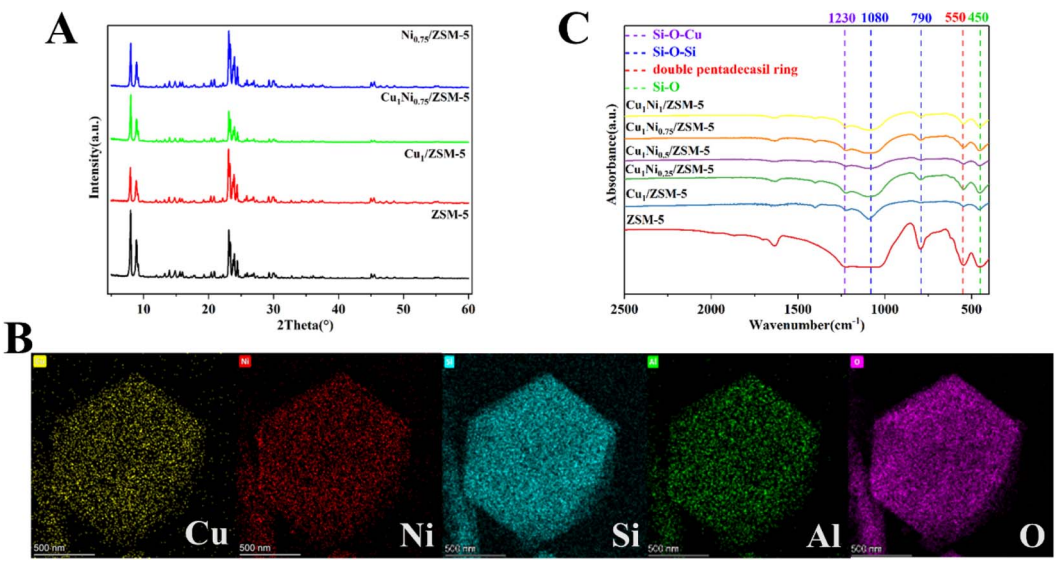

Fig. 2 (A) XRD patterns of ZSM-5, Cu_1/ZSM-5, $Cu_1Ni_{0.75}$/ZSM-5, and $Ni_{0.75}$/ZSM-5 catalysts. (B) STEM-EDS elemental mappings of $Cu_1Ni_{0.75}$/ZSM-5 catalyst. (C) The FT-IR spectrum of Cu_xNi_y/ZSM-5 catalysts in the range of 400–2500 cm^{-1}.

through the EDS mapping (Fig. 2B), similarly, the ICP-OES results confirmed the existence of Cu and Ni elements, which explained the high dispersibility of Cu and Ni in zeolite support. The TEM images were displayed in Fig. S8,† which indicated that CuNi existed on the surface of ZSM-5 zeolite in the form of nanoparticles. Next, the structure of Cu_xNi_y/ZSM-5 catalysts were further studied by FT-IR (Fig. 2C). The 550 cm^{-1} vibration band was assigned to the unique vibration way of double pentadecasil ring, a typical characteristics of ZSM-5 zeolite, which showed that the loading of metal did not damage the structure of the ZSM-5 zeolite.[38] The 462 cm^{-1} signal is attributed to the bending vibration of Si(Al)–O bonds, the peaks at 790 cm^{-1},1080 cm^{-1} and 1230 cm^{-1} were assigned to the asymmetric stretching vibrational of Si–O–Si bonds.[39] After the loading of metal (Cu or CuNi), the 1080 cm^{-1} and 1230 cm^{-1} bands become sharper, which marks the substitution of metal atoms in the ZSM-5 zeolite framework to form Si–O–Cu bonds.[40] According to previous reports, this was attributed to the alkalinity of the ammonia evaporation method led to partial desilication, and then copper atoms replaced the position of silicon atoms to form Si–O–Cu bonds in the zeolite framework.[41–43]

The EDS mapping images show the distribution of Cu and Ni elements to be uniformed (Fig. 2B). To further study the elemental coordination information of Cu and Ni, XPS analysis was used to analyze chemical states (Fig. 3A). The Cu 2p signal of the Cu_1Ni_y/ZSM-5 catalysts can be fitted into two peaks located at 932.6 and 933.8 eV, respectively for Cu^I and Cu^{II} species.[44,45] In addition, the low intensity of Cu^{II} satellite peak located at 943.0 eV may be due to the high dispersibility of Cu^{II} in the zeolite,[46,47] which has been previously demonstrated by XRD, ICP-OES and EDS mapping. When only Cu was loaded, Cu^{II} sites are predominant on the catalyst, with only a small portion of Cu^I sites present. As the loading of Ni increases, the Cu^I/Cu^{II} ratio rapidly increased from 0.19 to 0.86 (Table 1),

Table 1 Cu 2p XPS results of the Cu_1Ni_y/ZSM-5 catalysts

		Binding energy		
Entry	Sample	Cu^I	Cu^{II}	Cu^I/Cu^{II} ratio
1	Cu_1/ZSM-5	932.6	933.8	0.19
2	$Cu_1Ni_{0.25}$/ZSM-5	932.6	933.8	0.27
3	$Cu_1Ni_{0.5}$/ZSM-5	932.6	933.8	0.53
4	$Cu_1Ni_{0.75}$/ZSM-5	932.6	933.8	0.70
5	Cu_1Ni_1/ZSM-5	932.6	933.8	0.86

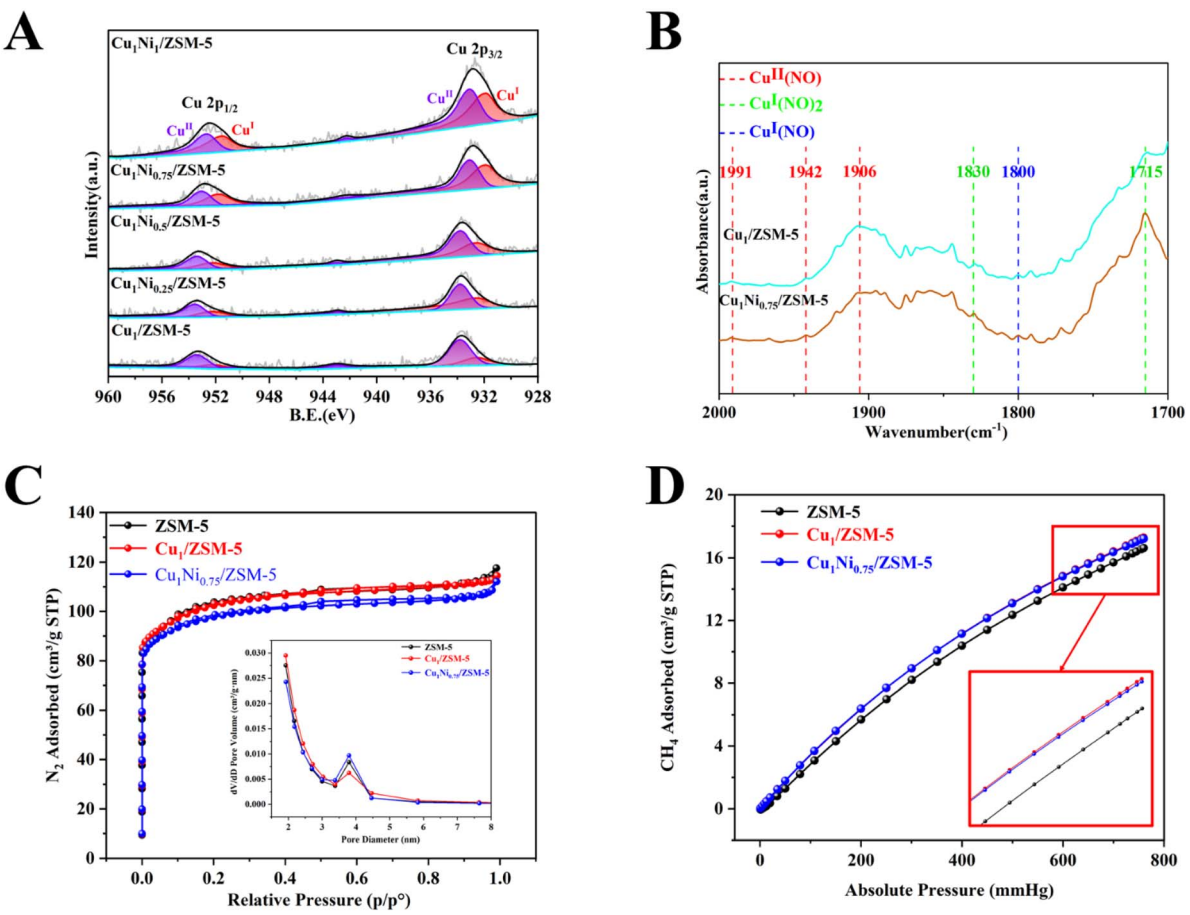

Fig. 3 (A) Cu 2p XPS spectra of different Cu_1Ni_y/ZSM-5 catalysts. (B) *In situ* NO-DRIFTS spectra of Cu_1/ZSM-5 and $Cu_1Ni_{0.75}$/ZSM-5 catalysts at room temperature. (C) N_2 adsorption–desorption isotherms of the ZSM-5, Cu_1/ZSM-5 and $Cu_1Ni_{0.75}$/ZSM-5 catalysts at 77 K. (D) Adsorption–desorption isotherms for CH_4 in ZSM-5, Cu_1/ZSM-5 and $Cu_1Ni_{0.75}$/ZSM-5 catalysts at 283 K.

correspondingly, the Ni^{II}/Ni^{0} ratio increased from 0.31 to 1.25 (Table S5†), which means that the ratio of Cu^{I} and Ni^{II} increased.[48] Combined with the limited reactivity over Ni/ZSM-5 sample, it could be assumed that Cu^{I} plays the dominating role in DOMM reaction. Moreover, the variation of binding energy for Cu 2p and Ni 2p indicates electron transfer from Ni to Cu(Fig. S10†). The electronic perturbation of Cu by Ni is known as ligand effect, these currently electron-rich Cu sites could form strong polar interactions with carbon atoms in methane molecules, which helps to break the symmetry and stability of C–H bonds, ergo boosting CH_4 cleavage to $*CH_3$. And the increase of $*CH_3$ could be confirmed through *in situ* CH_4-DRIFTS spectra described below (Fig. 4A).

In situ NO-DRIFTS spectra was used to further distinguish Cu^{I} and Cu^{II} sites (Fig. 3B). The signal at 1800 cm^{-1} was identified as the absorption peak of $Cu^{I}(NO)$. The signals at 1715 cm^{-1} and 1830 cm^{-1} were attributed to the absorption peaks of $Cu^{I}(NO)_2$, correspondingly, the absorption peaks at 1906 cm^{-1}, 1942 cm^{-1} and 1991 cm^{-1} related to $Cu^{II}(NO)$,[30,49,50] which indicated the coexistence of Cu^{I} and Cu^{II} sites in the Cu_xNi_y/ZSM-5 catalysts. Meanwhile, the XRD, FT-IR, XPS and *In situ* NO-DRIFTS comparison of the recycled $Cu_1Ni_{0.75}$/ZSM-5 was carried out (Fig. S11†). The Cu^{I}/Cu^{II} ratio of recycled $Cu_1Ni_{0.75}$/ZSM-5 was 0.69, which was close to fresh $Cu_1Ni_{0.75}$/ZSM-5 (0.70). These characterizations of $Cu_1Ni_{0.75}$/ZSM-5 after reaction remain almost the same as the fresh samples, confirming the stability of catalyst structure.

N_2/CH_4 isotherm adsorption–desorption experiments results were showed in Fig. 3C, D and Table S6.† Compared with ZSM-5, the BET surface area remained almost unchanged and the microporous structure was slightly lost, but, the adsorption of CH_4 by Cu_1/ZSM-5 was significantly improved, which was clearly attributed to the presence of Cu sites. When Ni are further introduced, the BET specific surface area and total pore volume of the $Cu_1Ni_{0.75}$/ZSM-5 catalyst were slightly reduced, which may be due to the loading of Ni caused changes in the physical structure of ZSM-5 carrier, as the length of Ni–O bonds (~2.0 Å) does not match that of Si–O bonds (~1.6 Å). Therefore, this substitution of Ni for Si would present a minor variation of the shape and size of ZSM-5 channels. This could explain the decrease in activity when the loading of Ni exceeds 0.75 wt%, which is that the excessive Ni species blocked the micropores, thereby hindering the transfer of reactants. In addition, there was no significant change in the adsorption of CH_4 by $Cu_1Ni_{0.75}$/ZSM-5 compared to Cu_1/ZSM-5.

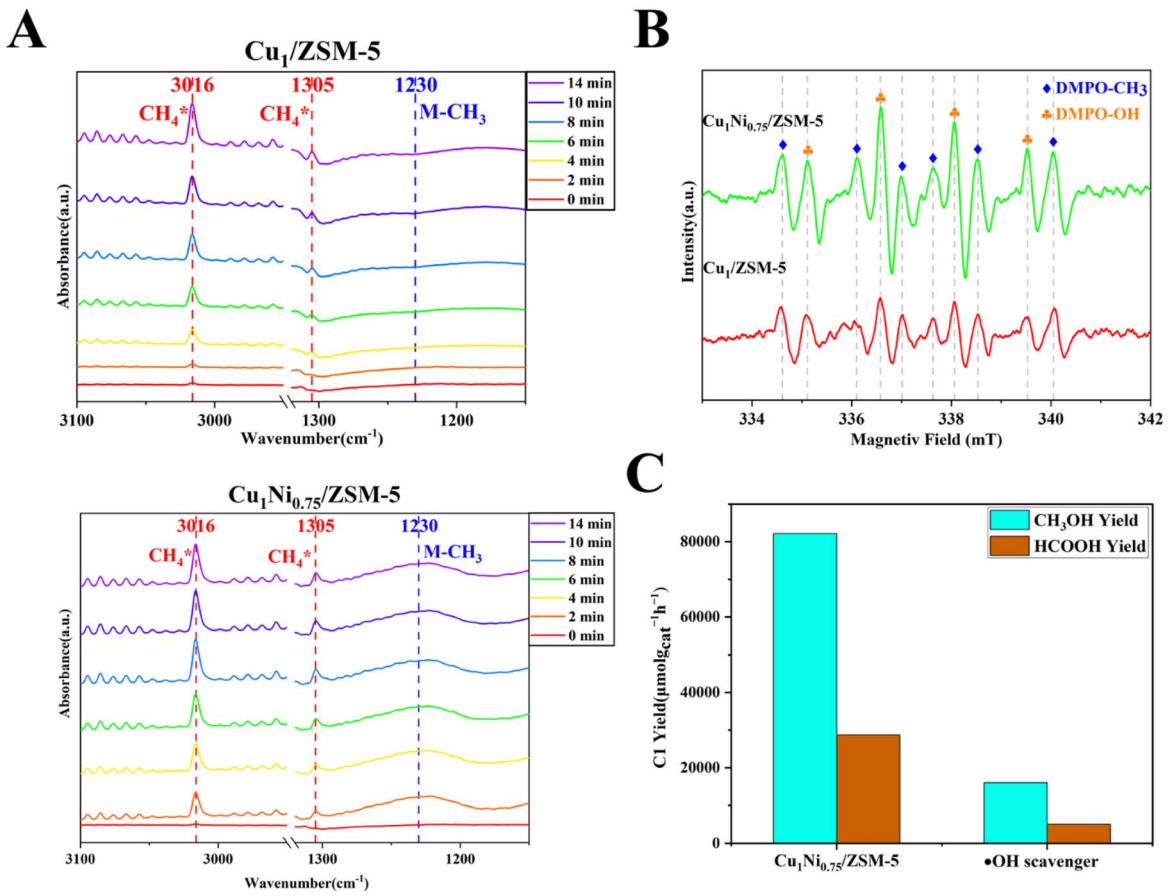

Fig. 4 (A) *In situ* DRIFTS spectra of CH_4 adsorption at 80 °C for Cu_1/ZSM-5 and $Cu_1Ni_{0.75}$/ZSM-5 catalysts. (B) EPR free radical capture experiments using DMPO as the radical trapping agent over Cu_1/ZSM-5 and $Cu_1Ni_{0.75}$/ZSM-5 catalysts. (C) C1 yield during direct oxidation of methane to methanol using ascorbic acid as free radical scavenger.

3.3. Reaction mechanism

The coexistence of Cu^{I} and Cu^{II} sites in the Cu_xNi_y/ZSM-5 catalysts has been confirmed, but their effect on the DOMM reaction has not been determined yet. Therefore, *in situ* CH_4-DRIFTS spectra were used to detect the function of the Cu^{II} and Cu^{I} sites (Fig. 4A). Several strong absorption peaks attributed to $*CH_4$ (3016 cm^{-1} and 1305 cm^{-1})[51–53] and formed M–CH_3 (1230 cm^{-1}, M:Cu or Ni) 33 can be detected on $Cu_1Ni_{0.75}$/ZSM-5 catalyst with abundant Cu^{I} sites. While the Cu_1/ZSM-5 catalyst with more Cu^{II} sites also had the absorption peaks of CH_4^* at 3016 cm^{-1} and 1305 cm^{-1}, but the absorption peaks at Cu_1/ZSM-5 catalyst were significantly lower than that at $Cu_1Ni_{0.75}$/ZSM-5 catalyst, which showed Cu^{I} sites are apparently conducive to methane adsorption (Fig. S12†). In addition, the absorption peak of M–CH_3 at 1230 cm^{-1} was nearly invisible compared to that at $Cu_1Ni_{0.75}$/ZSM-5 catalyst, again testified the constrained CH_4 activation ability of pure Cu sample with limited Cu^{I} (Fig. S13†). We believe that the reason for the above results is: the $Cu_1Ni_{0.75}$/ZSM-5 catalyst with the majority of Cu^{I} sites has a stronger ability to promote the breaking of the first C–H bonds of CH_4. The $*CH_3$ adsorbed on metal sites could react with $^{\cdot}OH$ in the liquid phase to generate CH_3OH, thus, explaining the high yield of CH_3OH in $Cu_1Ni_{0.75}$/ZSM-5 for its metal sites were more valid to form $*CH_3$. In addition, no signals for OCH_3* species (2836 cm^{-1} and 1047 cm^{-1}) were found,[54–56] which showed $*CH_3$ did not tend to adsorb on O sites, but rather tended to adsorb on metal sites (Fig. S14†). Combining N_2/CH_4 isotherm adsorption–desorption experiments results and *in situ* CH_4-DRIFTS spectra, it was speculated that CH_4 was adsorbed on Cu sites, and Cu^{I} sites had better ability to promote CH_4 adsorption, CH_4 activation and CH_3OH generation compared to Cu^{II} sites. Therefore, we found that the Cu^{I} sites plays a role in activating CH_4, and CH_4^* adsorbs onto them at the beginning of the DOMM reaction and generating initial $*CH_3$. Subsequently, $*CH_3$ was converted to $^{\cdot}CH_3$ under the induction of a free radical rich aqueous solution, and then combined with $^{\cdot}OH$ to generate CH_3OH.

Usually, the mechanisms of the DOMM reaction can be divided into free radical mechanism[57,58] and non-free mechanism[59,60] according to the different intermediate transition species. In the control experiment without H_2O_2, there were no products (Fig. S3†). Moreover, the activity of DOMM reaction was significantly limited when there was no catalyst or only pure ZSM-5 zeolite. Next, the reaction activities were greatly enhanced when ZSM-5 support was loaded with Cu or CuNi, thus, the DMPO spin-trapping Electron Paramagnetic Resonance experiments were used to give in-depth insight into the behaviors of free radicals during the reaction process (Fig. 4B). The presence of $^{\cdot}CH_3$ and $^{\cdot}OH$ could be clearly observed through free radical capture experiments using DMPO, and the concentrations of $^{\cdot}CH_3$ and $^{\cdot}OH$ in the DOMM reaction catalyzed by $Cu_1Ni_{0.75}$/ZSM-5 were significantly higher than those catalyzed by Cu_1/ZSM-5, which explained $Cu_1Ni_{0.75}$/ZSM-5 catalyst had excellent ability to promote the breaking of C–H bonds in CH_4 to form $*CH_3$ and the dissociation of H_2O_2 to produce $^{\cdot}OH$, and then the $^{\cdot}OH$ radicals generated by H_2O_2 abstracted the metal adsorbed $*CH_3$ to $^{\cdot}CH_3$. In addition, a small amount of $^{\cdot}OH$ radicals was detected over Cu_1/ZSM-5, indicating that the contribution of Cu species to the generation of $^{\cdot}OH$ radicals was limited, while a large amount of $^{\cdot}OH$ was formed over $Cu_1Ni_{0.75}$/ZSM-5, indicating that the combination of Cu and Ni species had better ability to promote the decomposition of H_2O_2 to produce $^{\cdot}OH$ radicals compared to single Cu species. This phenomenon was known as the Fenton-like reaction, which explained the high $^{\cdot}OH$ concentration over $Cu_1Ni_{0.75}$/ZSM-5.[61]

In order to explore the source of another important C1 product HCOOH, subsequent oxidation experiments were conducted to determine the order of its production with CH_3OH, specifically, 40 mL aqueous solution containing 0.01 M CH_3OH and 0.5 M H_2O_2 and 30 bar N_2 was used. The products (0.009 M CH_3OH and 0.001 M HCOOH), indicated that HCOOH was produced by CH_3OH peroxidation, *i.e.* CH_4 to HCOOH is a two-step reaction ($CH_4 \rightarrow CH_3OH \rightarrow HCOOH$) (Fig. S15†).

The pathway of DOMM reaction under the influence of various free radicals was studied by combining the volcano-shaped curve of methanol yield and characterization method. Firstly, $*CH_4$ adsorbed onto metal sites at the beginning of the DOMM reaction and generated initial $*CH_3$. Subsequently, $*CH_3$ was converted to $^{\cdot}CH_3$ under the induction of a free radical rich aqueous solution. Then, we found that the yield of CH_3OH significantly decreased when $^{\cdot}OH$ was quenched, which confirmed the hypothesis that CH_3OH was composed of $^{\cdot}OH$ capturing $^{\cdot}CH_3$. Finally, we believed that a small portion of CH_3OH was further oxidized to form the byproduct HCOOH under the influence of $^{\cdot}OH$ based on the control experiment using CH_3OH as the sole carbon source and corresponding $^{\cdot}OH$ quenching experiment as described above (Fig. S15†).

A comprehensive and feasible reaction pathway for direct oxidation of methane to methanol over Ni-promoted Cu/ZSM-5 using H_2O_2 as oxidant had been proposed according to a series of controlled experiments, EPR free radical capture experiments, *in situ* CH_4-DRIFTS spectra and free radical quenching experiments. In the liquid-phase system containing Ni-Promoted Cu/ZSM-5 and H_2O_2, Cu^{I} promoted the adsorption of methane and efficiently polarized the first C–H bond of methane to form $*CH_3$. Subsequently, $*CH_3$ was converted to $^{\cdot}CH_3$ under the induction of a free radical rich aqueous solution, and then combined with $^{\cdot}OH$ radicals generated by H_2O_2 to generate the target product (CH_3OH) of the DOMM reaction, but partial CH_3OH would be attacked by $^{\cdot}OH$ and undergo excessive oxidation to generate HCOOH.

4 Conclusion

In conclusion, we have prepared a series of Cu_xNi_y/ZSM-5 catalysts with different Ni loadings through the ammonia evaporation method for the direct oxidation of methane to methanol using H_2O_2 as the oxidant. A volcano-type catalytic performance was exhibited with the increase of Ni loading amounts, where the maximum catalytic activity appeared at $Cu_1Ni_{0.75}$/ZSM-5 with a CH_3OH yield of 82 162 μmol g_{cat}^{-1} h^{-1} and CH_3OH selectivity of 74%, which was obviously superior

than monometallic Cu_1/ZSM-5 catalyst. We had explained the reason why the addition of Ni effectively promoted the catalytic activity of Cu/ZSM-5 for methane conversion through a combination of various experiments (especially the control experiments and $^{\bullet}OH$ partial quenching experiment) and characterization methods: on the one hand, Ni promoted the conversion of Cu^{II} to Cu^{I}, these currently electron-rich Cu sites (Cu^{I} sites) could form strong polar interactions with carbon atoms in methane molecules, which helped to break the symmetry and stability of C–H bonds, ergo boosting CH_4 cleavage to $*CH_3$; on the other hand, the combination of Cu and Ni species, instead of single Cu species, promoted the decomposition of H_2O_2 to produce more $^{\bullet}OH$ radicals, thus, the methanol yield increased accordingly. Correspondingly, a small amount of methanol would undergo excessive oxidation to form formic acid under the action of $^{\bullet}OH$ radicals. This work provides useful and valuable opinion into the direct oxidation of methane to methanol over the metal-zeolite catalysts in the H_2O_2 liquid phase system, and opens up whole new vistas for the design of highly efficient metal-zeolite catalysts for direct oxidation of methane to methanol.

Data availability

The data supporting this article have been included as part of the ESI.†

Author contributions

W. L. and Z. S. conceived and supervised the research. Z. S. designed and performed the experiments and data analysis. Z. S. and J. J. wrote the paper. All authors discussed the results and commented on the paper.

Conflicts of interest

There are no conflicts to declare.

Acknowledgements

This work was supported by the Anhui Natural Science Foundation (2408085ME143), Key Research and Development Projects in Anhui Province (2022107020013) and the Institute of Energy, the Hefei Comprehensive National Science Center under Grant No. 21KZS219.

References

1 L. He, Y. Fan, J. Bellettre, J. Yue and L. Luo, *Renewable Sustainable Energy Rev.*, 2020, **119**, 109589.
2 D. Allen, *Acc. Chem. Res.*, 2016, **49**, 1344–1350.
3 Y. Xu, X. Li, J. Gao, J. Wang, G. Ma, X. Wen, Y. Yang, Y. Li and M. Ding, *Science*, 2021, **371**, 610–613.
4 A. K. M. K. Aurnob, K. Ding, D. R. Kauffman and J. J. Spivey, *Appl. Catal., B*, 2023, **322**, 122107.
5 T. N. Le, T. B. N. Le, P. T. Nguyen, T. T. Nguyen, Q. N. Tran, T. T. Nguyen, Y. Kawazoe, T. B. Phan and D. M. Nguyen, *RSC Adv.*, 2023, **13**, 15926–15933.
6 A. I. Olivos-Suarez, À. Szécsényi, E. J. M. Hensen, J. Ruiz-Martinez, E. A. Pidko and J. Gascon, *ACS Catal.*, 2016, **6**, 2965–2981.
7 B. An, Z. Li, Z. Wang, X. Zeng, X. Han, Y. Cheng, A. M. Sheveleva, Z. Zhang, F. Tuna, E. J. L. McInnes, M. D. Frogley, A. J. Ramirez-Cuesta, L. S. Natrajan, C. Wang, W. Lin, S. Yang and M. Schröder, *Nat. Mater.*, 2022, **21**, 932–938.
8 M. H. Mahyuddin, Y. Shiota, A. Staykov and K. Yoshizawa, *Acc. Chem. Res.*, 2018, **51**, 2382–2390.
9 K. Aasberg-Petersen, I. Dybkjær, C. V. Ovesen, N. C. Schjødt, J. Sehested and S. G. Thomsen, *J. Nat. Gas Sci. Eng.*, 2011, **3**, 423–459.
10 C. Palmer, D. C. Upham, S. Smart, M. J. Gordon, H. Metiu and E. W. McFarland, *Nat. Catal.*, 2020, **3**, 83–89.
11 K. T. Dinh, M. M. Sullivan, K. Narsimhan, P. Serna, R. J. Meyer, M. Dinca and Y. Roman-Leshkov, *J. Am. Chem. Soc.*, 2019, **141**, 11641–11650.
12 L. Luo, J. Luo, H. Li, F. Ren, Y. Zhang, A. Liu, W. Li and J. Zeng, *Nat. Commun.*, 2021, **12**, 1218.
13 Y. Fan, W. Zhou, X. Qiu, H. Li, Y. Jiang, Z. Sun, D. Han, L. Niu and Z. Tang, *Nat. Sustain.*, 2021, **4**, 509–515.
14 C. Feng, S. Zuo, M. Hu, Y. Ren, L. Xia, J. Luo, C. Zou, S. Wang, Y. Zhu, M. Rueping, Y. Han and H. Zhang, *Nat. Commun.*, 2024, **15**, 9088.
15 Z. Jin, L. Wang, E. Zuidema, K. Mondal, M. Zhang, J. Zhang, C. Wang, X. Meng, H. Yang, C. Mesters and F. S. Xiao, *Science*, 2020, **367**, 193–197.
16 R. Serra-Maia, F. M. Michel, T. A. Douglas, Y. Kang and E. A. Stach, *ACS Catal.*, 2021, **11**, 2837–2845.
17 M. Li, J. Shan, G. Giannakakis, M. Ouyang, S. Cao, S. Lee, L. F. Allard and M. Flytzani-Stephanopoulos, *Appl. Catal., B*, 2021, **292**, 120124.
18 Y. Xi and A. Heyden, *ACS Catal.*, 2019, **9**, 6073–6079.
19 J. Li, P. Yan, K. Li, J. You, H. Wang, W. Cui, W. Cen, Y. Chu and F. Dong, *J. Mater. Chem. A*, 2019, **7**, 17014–17021.
20 J. Baek, B. Rungtaweevoranit, X. Pei, M. Park, S. C. Fakra, Y. Liu, R. Matheu, S. A. Alshmimri, S. Alshehri, C. A. Trickett, G. A. Somorjai and O. M. Yaghi, *J. Am. Chem. Soc.*, 2018, **140**, 18208–18216.
21 M. C. Simons, S. D. Prinslow, M. Babucci, A. S. Hoffman, J. Hong, J. G. Vitillo, S. R. Bare, B. C. Gates, C. C. Lu, L. Gagliardi and A. Bhan, *J. Am. Chem. Soc.*, 2021, **143**, 12165–12174.
22 Y. Xu, D. Wu, Q. Zhang, P. Rao, P. Deng, M. Tang, J. Li, Y. Hua, C. Wang, S. Zhong, C. Jia, Z. Liu, Y. Shen, L. Gu, X. Tian and Q. Liu, *Nat. Commun.*, 2024, **15**, 564.
23 A. Li, T. Wang, C. Li, Z. Huang, Z. Luo and J. Gong, *Angew. Chem., Int. Ed.*, 2019, **58**, 3804–3808.
24 B. Wang, F. Yang, Y. Dong, Y. Cao, J. Wang, B. Yang, Y. Wei, W. Wan, J. Chen and H. Jing, *Chem. Eng. J.*, 2020, **396**, 125255.
25 L. Que and W. B. Tolman, *Nature*, 2008, **455**, 333–340.

26 X. Liu, C. Wang, J. Zhou, C. Liu, Z. Liu, J. Shi, Y. Wang, J. Teng and Z. Xie, *Chem. Soc. Rev.*, 2022, **51**, 8174–8200.
27 Y. Chai, W. Dai, G. Wu, N. Guan and L. Li, *Acc. Chem. Res.*, 2021, **54**, 2894–2904.
28 H. M. Rhoda, A. J. Heyer, B. E. R. Snyder, D. Plessers, M. L. Bols, R. A. Schoonheydt, B. F. Sels and E. I. Solomon, *Chem. Rev.*, 2022, **122**, 12207–12243.
29 M. A. Newton, A. J. Knorpp, V. L. Sushkevich, D. Palagin and J. A. van Bokhoven, *Chem. Soc. Rev.*, 2020, **49**, 1449–1486.
30 V. L. Sushkevich, D. Palagin, M. Ranocchiari and J. A. van Bokhoven, *Science*, 2017, **356**, 523.
31 J. Jin, W. Li, L. Zhang, L. Zhu, L. Wang and Z. Zhou, *J. Colloid Interface Sci.*, 2023, **645**, 964–973.
32 K. T. Dinh, M. M. Sullivan, P. Serna, R. J. Meyer, M. Dincă and Y. Román-Leshkov, *ACS Catal.*, 2018, **8**, 8306–8313.
33 H. Zhang, P. Han, D. Wu, C. Du, J. Zhao, K. H. L. Zhang, J. Lin, S. Wan, J. Huang, S. Wang, H. Xiong and Y. Wang, *Nat. Commun.*, 2023, **14**, 7705.
34 T. Yu, Z. Li, L. Lin, S. Chu, Y. Su, W. Song, A. Wang, B. M. Weckhuysen and W. Luo, *ACS Catal.*, 2021, **11**, 6684–6691.
35 L. Wang, J. Jin, W. Li, C. Li, L. Zhu, Z. Zhou, L. Zhang, X. Zhang and L. Yuan, *Energy Environ. Sci.*, 2024, **17**, 9122–9133.
36 B. Yu, L. Cheng, S. Dai, Y. Jiang, B. Yang, H. Li, Y. Zhao, J. Xu, Y. Zhang, C. Pan, X. M. Cao, Y. Zhu and Y. Lou, *Adv. Sci.*, 2023, **10**, 2302143.
37 S. Bai, Y. Xu, P. Wang, Q. Shao and X. Huang, *ACS Catal.*, 2019, **9**, 6938–6944.
38 H. Liu, H. Liu, J. Hu, W. Zhong, Z. Hu and H. Wang, *J. Anal. Appl. Pyrolysis*, 2024, **181**, 106608.
39 E. Yuan, K. Zhang, G. Lu, Z. Mo and Z. Tang, *J. Ind. Eng. Chem.*, 2016, **42**, 142–148.
40 S. K. Jesudoss, J. Judith Vijaya, K. Kaviyarasu, P. Iyyappa Rajan, S. Narayanan and L. John Kennedy, *J. Photochem. Photobiol., B*, 2018, **186**, 178–188.
41 Y. Meng, H. C. Genuino, C. Kuo, H. Huang, S. Chen, L. Zhang, A. Rossi and S. L. Suib, *J. Am. Chem. Soc.*, 2013, **135**, 8594–8605.
42 J. Gong, H. Yue, Y. Zhao, S. Zhao, L. Zhao, J. Lv, S. Wang and X. Ma, *J. Am. Chem. Soc.*, 2012, **134**, 13922–13925.
43 J. Pang, M. Zheng, C. Wang, X. Yang, H. Liu, X. Liu, J. Sun, Y. Wang and T. Zhang, *ACS Catal.*, 2020, **10**, 13624–13629.
44 L. Artiglia, V. L. Sushkevich, D. Palagin, A. J. Knorpp, K. Roy and J. A. van Bokhoven, *ACS Catal.*, 2019, **9**, 6728–6737.
45 H. Xue, X. Guo, T. Meng, Q. Guo, D. Mao and S. Wang, *ACS Catal.*, 2021, **11**, 7702–7718.
46 E. P. Hessou, M. Badawi, L. Valentin, G. Atohoun, S. Dzwigaj, M. Calatayud and F. Tielens, *Top. Catal.*, 2022, **65**, 848–858.
47 A. Corma, A. Palomares and F. Marquez, *J. Catal.*, 1997, **170**, 132–139.
48 Y. Chen, B. Qiu, Y. Liu and Y. Zhang, *Appl. Catal., B*, 2020, **269**, 118801.
49 F. Giordanino, P. N. R. Vennestrøm, L. F. Lundegaard, F. N. Stappen, S. Mossin, P. Beato, S. Bordiga and C. Lamberti, *Dalton Trans.*, 2013, **42**, 12741.
50 Z. Zhou, M. Miao, W. Li, J. Jin, L. Wang, L. Zhang and L. Yuan, *Mol. Catal.*, 2024, **562**, 114237.
51 J. Ding, Z. Teng, X. Su, K. Kato, Y. Liu, T. Xiao, W. Liu, L. Liu, Q. Zhang, X. Ren, J. Zhang, Z. Chen, O. Teruhisa, A. Yamakata, H. Yang, Y. Huang, B. Liu and Y. Zhai, *Chem*, 2023, **9**, 1017–1035.
52 X. Sun, X. Chen, C. Fu, Q. Yu, X. Zheng, F. Fang, Y. Liu, J. Zhu, W. Zhang and W. Huang, *Nat. Commun.*, 2022, **13**, 6677.
53 C. Wang, Y. Xu, L. Xiong, X. Li, E. Chen, T. J. Miao, T. Zhang, Y. Lan and J. Tang, *Nat. Commun.*, 2024, **15**, 7535.
54 C. Zhang, L. Wang, Y. Chen, X. He, Y. Song, O. M. Gazit and Z. Zhong, *Chem. Eng. J.*, 2023, **475**, 146102.
55 X. Xiao, G. Wang, X. Cai, H. Liu, F. Si, H. Wang, T. Hou and Y. Li, *Chem. Eng. J.*, 2024, **498**, 155404.
56 J. D. Jiménez, P. G. Lustemberg, M. Danielis, E. Fernández-Villanueva, S. Hwang, I. Waluyo, A. Hunt, D. Wierzbicki, J. Zhang, L. Qi, A. Trovarelli, J. A. Rodriguez, S. Colussi, M. V. Ganduglia-Pirovano and S. D. Senanayake, *J. Am. Chem. Soc.*, 2024, **146**, 25986–25999.
57 X. Song, C. Basheer and R. N. Zare, *J. Am. Chem. Soc.*, 2023, **145**, 27198–27204.
58 Q. Zhou, X. Tan, X. Wang, Q. Zhang, C. Qi, H. Yang, Z. He, T. Xing, M. Wang, M. Wu and W. Wu, *ACS Catal.*, 2024, **14**, 955–964.
59 H. Lee, C. Kwon, C. Keum, H. Kim, H. Lee, B. Han and S. Lee, *Chem. Eng. J.*, 2022, **450**, 138472.
60 Z. Fang, M. Huang, B. Liu, F. Jiang, Y. Xu and X. Liu, *J. Catal.*, 2022, **405**, 1–14.
61 M. Shen, Z. Huang, L. Qiu, Z. Chen, X. Xiao, X. Mo and L. Cui, *J. Cleaner Prod.*, 2020, **268**, 122174.